Rate Constant Measurements for the Reaction of HO$_2$ with O$_3$ from 200 to 300 K Using a Turbulent Flow Reactor[†]

Scott C. Herndon,* Peter W. Villalta,[‡] David D. Nelson, John T. Jayne, and Mark S. Zahniser*

Aerodyne Research, Inc., Center for Atmospheric and Environmental Chemistry, Billerica, Massachusetts 01821

The rate constant for the reaction of HO$_2$ with O$_3$ was measured using a turbulent flow reactor with tunable diode laser absorption detection of HO$_2$. Two separate methods were used to determine k_1 from the pseudo-first-order decay of HO$_2$ in excess O$_3$. The isotopic labeling method used H^{18}O$_2$ in excess ^{16}O$_3$ to avoid reformation of the reactant. The OH scavenger method used trifluorochloroethylene to remove the OH product and prevent re-formation of HO$_2$. The turbulent flow reactor allowed measurements at temperatures between 297 and 197 K at total pressures from 80 to 175 Torr, spanning a wide range of stratospheric conditions. The temperature-dependent rate constant is given by the three-term expression $k_1(T) = \{(103 \pm 57) \exp[-(1323 \pm 160)/T] + 0.88\} \times 10^{-15}$ cm^3 molecule^{-1} s^{-1}, reflecting its non-Arrhenius behavior at low temperatures. These results demonstrate that the catalytic destruction of lower stratospheric O$_3$ by HO$_x$ radicals (OH and HO$_2$) may proceed faster than current models predict. The rate constant at 295 K is $(2.0 \pm 0.2) \times 10^{-15}$ cm^3 molecule^{-1} s^{-1}.

Introduction

The cycling of HO$_x$ (HO$_x$ = OH + HO$_2$) through reactions 1 and 2 represents the dominant O$_3$ loss process occurring in

$$HO_2 + O_3 \xrightarrow{k_1} OH + 2O_2 \qquad (R1)$$

$$OH + O_3 \xrightarrow{k_2} HO_2 + O_2 \qquad (R2)$$
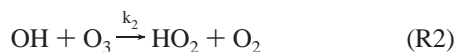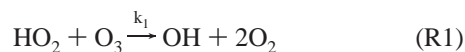
the lower stratosphere over much of the globe.[1] Reaction 1 is the rate-limiting step in this HO$_x$-only ozone destruction cycle. The atmospheric impact of reaction 1 on O$_3$ loss, however, is coupled to the ozone destruction associated with NO$_x$ (NO$_x$ = NO + NO$_2$) and reactive halogen.[2,3]

A difficulty with direct measurements of k_1 under pseudo-first-order conditions with respect to HO$_2$ is the rapid regeneration of HO$_2$ due to this very cycle. Previous studies[4−6] have used an OH scavenger or have used isotopic labeling[7] of the HO$_2$ in order to determine k_1.

The previous work indicates that strict Arrhenius behavior is not observed in the temperature dependence of k_1. At lower temperatures the rate constant may be higher than would be predicted by extrapolation of the data taken above 230 K. Reaction 1 proceeds through two channels, corresponding to transfer of the hydrogen atom (major) or the transfer of the terminal oxygen atom in HO$_2$ (minor),[7,8] but the present understanding of the associated mechanisms does not predict the temperature dependence of k_1.

Although this rate constant, k_1, is most frequently utilized in atmospheric modeling, there have been no previous direct measurements of k_1 below 233 K, even though lower stratospheric temperatures can be as low as 185 K. The turbulent

flow reactor used in this study allows direct measurement of k_1 at stratospheric temperatures and pressures. Both isotopic labeling of reactant HO$_2$ and an OH scavenger were used to reduce the effects of secondary chemistry. In conventional low-pressure laminar flow tubes, the loss of HO$_2$ to the walls is sufficient to complicate measurements of k_1, particularly at low temperatures. In the high-pressure turbulent flow technique, there is limited mass exchange between the turbulent core and the viscous sublayer, which forms near the wall. Under these circumstances, the measured wall loss rate constants are less dependent on wall temperature. This property of the turbulent flow reactor allows the study of HO$_2$ kinetics at temperatures less than 240 K.

Experimental Section

Turbulent Flow Approach. The use of a turbulent flow reactor to study chemical kinetics was developed by Seeley and co-workers.[9,10] The technique has been used to study the kinetics of several reactions.[11,12] It is a relatively new method, though, and a short description of the technique will be presented here to facilitate the discussion of these results.

Conventional laminar flow tube reactors have a radially parabolic velocity profile where the gas velocity is greatest at the center of the tube and decreases by the square of the radial position to zero at the tube walls. The velocity fluctuations at any given radial point are low relative to the overall average velocity. This condition leads to a wide distribution of residence times for species that traverse the length of the tube, which is undesirable when attempting kinetics measurements. To circumvent this difficulty, the working pressure is held below ∼10 Torr in order to increase diffusional dispersion to such an extent that the radial concentration gradients in the flow tube are minimized. The use of molecular diffusion to overcome the gradient due to the flow profile characterizes the conventional low-pressure laminar flow approach to flow tube kinetics.

The Reynolds number for tubular flow is defined in eq 1.

$$R_e = \frac{2r\bar{v}\rho}{\eta} = \alpha\,\frac{QM}{r\eta} \qquad (1)$$

Equation 1 shows two representations of Re, where r is the tube radius, $\bar{v}$ is the average axial velocity of the gas, ρ is the density, η is the viscosity of the gas, α is a contant of proportionality, Q is the mass flow rate, and M is the molecular mass of the gas. In the case of tubular laminar flow, the Reynolds number is smaller than 900, usually <100 for flow tube kinetics. As the mass flow increases, the shear flow near the wall develops instabilities and velocity fluctuations occur which are greater than those present in laminar flow. The flow profiles in this regime are not well-defined, and this is referred to as the transition region between viscous and nonviscous flow. When $Re > 2000$, the flow becomes turbulent with a velocity profile which is more uniform than the parabolic profile characteristic of a laminar flow. The radial velocity profile of fully developed turbulent flow within the core is flat. Near the tube walls a viscous sublayer forms, and between the sublayer and the core a turbulent boundary layer develops. The radial motion in the core is the combination of molecular diffusion and small-scale turbulent mixing. Flow visualization studies[10] aimed at measuring the effective diffusivity of species in the core have found that in a fully developed turbulent flow the combined molecular and "eddy" diffusion is great enough to allow for radial mixing, but not so great that appreciable axial mixing occurs. Essentially, it is this result that allows chemical kinetics measurements to be conducted using a turbulent flow tube reactor.

When the one-dimensional form of the continuity equation is integrated using the boundary conditions appropriate for a reaction in a flow tube, the concentration of the reactive species, $\bar{c}$, is given by[9,13]

$$\bar{c}(z) = \bar{c}_0 \exp\!\left(\frac{-k_1{}^* z}{v_{\text{eff}}}\right) \qquad (2)$$

where z represents the distance down the flow tube ($c(0) = c_0$), v_{eff} is the gas velocity in the turbulent core, $k_1{}^*$ is the measured pseudo-first-order rate constant, and D_{eff} is the effective dispersion coefficient. In eq 2, an effective velocity of the turbulent core is used in place of the average velocity, which differs from the result using a fully laminar flow. The total pseudo-first-order rate coefficient is given by eq 3.[9,13] For the

$$k_1' = k_1{}^*\!\left(1 + \frac{D_{\text{eff}}\,k_1{}^*}{v_{\text{eff}}{}^2}\right) \qquad (3)$$

measurements presented here, $k_1 = k_1[O_3] + k_{\text{wall}}$. Equation 3 is very similar to that which arises in the instance of laminar flow. Other studies[14-16] have developed methods for measuring rate constants using a laminar flow at higher pressures either by determining the complete radial concentration profile or by applying corrections to an apparent temporal profile. When the detector samples the core of a turbulent flow reactor, the simple equations (2) and (3) may be applied; however, the effective velocity must be measured and the magnitude of D_{eff} must be determined.

Apparatus Description. A turbulent flow reactor coupled to a multipass cell designed for a long path length in a small volume has been used in the determination of k_1. A schematic of the instrument, with an expanded view of the area near the end of the injector, is presented in Figure 1. The flow reactor consists of a double jacketed Pyrex tube (2.5 cm i.d., 85 cm

long) which has been coated with a thin layer of halocarbon wax, emptying into a six-way cross. A sampling port with a 3 mm orifice was located inside the cross and directed a portion of the flow, via differential pumping, into a 55 cm long, 8.5 cm i.d. multipass cell. Nitrogen (Middlesex Gases 99.998%), from a liquid N_2 gas pack, served as the main flow tube carrier gas for the majority of the work presented here. Helium (Middlesex Gases 99.999%) was used at the carrier gas for the flow directed through the inner injector. Flows were measured using Tylan mass flow meters, which were periodically calibrated by measuring the rate of change of pressure into a known volume. Special care was taken to ensure these calibrations were done isothermally. Pressures in the reactor and multipass cell were measured using calibrated capacitance manometers. The temperature of the gas in the flow tube was measured using high gauge calibrated chromel–alumel thermocouples both at the end of the injector and just prior to the sampling port shown in Figure 1. The main carrier gas was precooled before passing into the main flow tube, and its temperature was maintained by a thermostated fluid which was circulated through the reactor jacket. The amount of precooling was controlled so that the temperature measured at the injector tip matched that measured prior to the sampling port. The flow through the injector was typically less than 6000 standard cubic centimeters per minute (sccm), while the total flow through the reactor was ~55 000 sccm. The pumping speed was adjusted such that the pressure in the flow tube ranged from 80 to 174 Torr and the average flow velocity of the gas varied from 850 to 2500 cm s^{-1}. The sampling pressure of 10 Torr was selected to optimize detection sensitivity at the point where pressure broadening and Doppler broadening are equal. The number density of O_3 dropped by a factor of 20 upon passage into the detector, and as a result, the extent of reaction occurring in the multipass cell relative to that in the flow tube was negligible. In flow tube experiments constraints such as the minimum distance between the injector tip and the detection region have an effect on the minimum detectable reaction times. This is sometimes referred to as the "end effect". The experimental conditions employed in the majority of this work result in an end effect, which is the equivalent of ~6 cm of flow tube distance.

A movable double injector was used to create and inject HO_2 to the main flow. A Beenaker style 2.5 GHz microwave discharge cavity[17] produced H atoms from trace amounts of H_2 (Wesco Gases 99.9995%) in the He carrier gas, which passed through the inner injector. This mixture flowed into the outer injector, which contained a sufficient flow of O_2 (Middlesex Gases 99.999%) to maintain more than 1×10^{17} molecules cm^3 O_2 in the diluted flow. The inner injector was recessed 25 cm from the end of the outer injector (see Figure 1), allowing the H atoms sufficient time to mix with the O_2/He and react to produce HO_2. Both the inner and outer injectors were coated with a halocarbon wax to reduce H and HO_2 losses on the injector walls.

Two Teflon "turbulizers" were mounted on the exterior of the outer injector as shown in Figure 1. These have the effect of enhancing the turbulent mixing between the injector and main gas flows. The gas velocities across the tube diameter were determined by measuring the difference between the static pressure and the impact pressure[18] using a Pitot tube. The impact pressure was determined using a 1 mm i.d. Pitot tube situated parallel to the direction of the flow. The static pressure was measured using a 1 mm i.d. Pitot tube with two holes normal to the direction of the tube. A differential manometer, 1 Torr full scale, was used to accurately measure Δp. The measure-
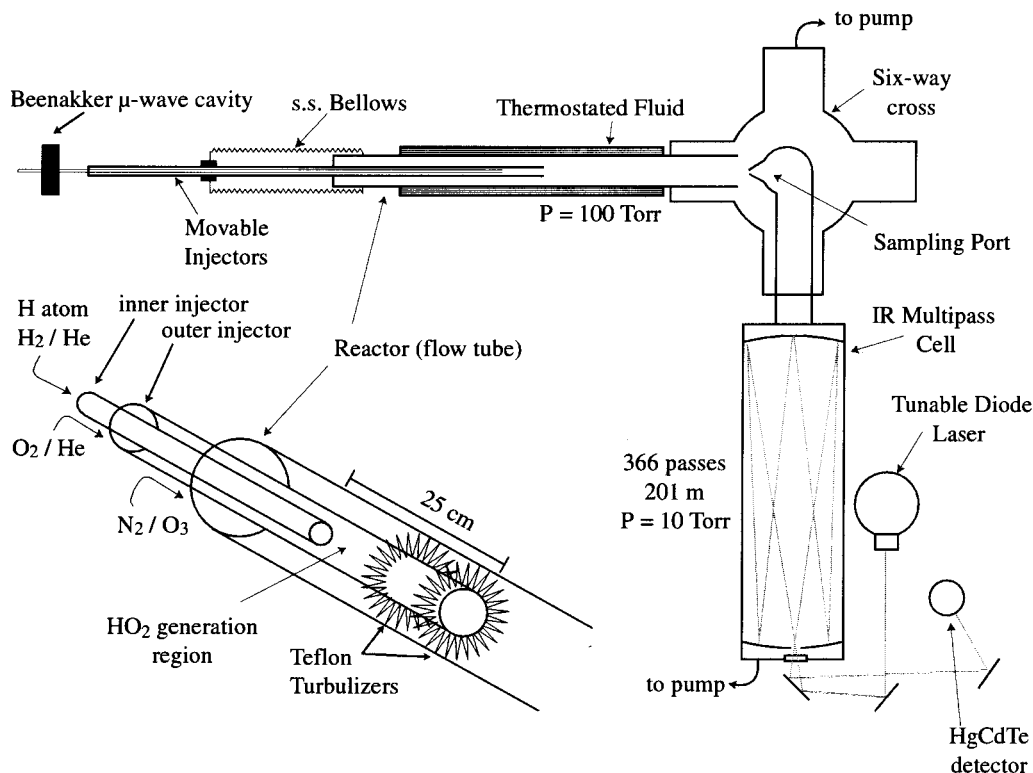
Figure 1. Schematic of the turbulent flow reactor coupled to a tunable diode laser. The inset shows detail of movable double injector with "turbulizers" mounted on the tip.

ments associated with the development of the turbulent flow will be discussed further in the results section.

Ozone was generated by passing O$_2$ through a corona arc discharge using a commercial ozone synthesizer. The ozone/O$_2$ mixture was passed through a 3 L glass bulb filled with silica gel. The O$_3$ was trapped and stored on the silica gel in an ethanol bath cooled to ~190 K. The ozone was delivered to the flow tube by passing a measured N$_2$ flow through the silica gel. This O$_3$/N$_2$ mixture flowed through an absorption cell with a path length of 0.165 cm where the concentration of O$_3$ was determined by ultraviolet absorption of the atomic Hg emission line at 253.7 nm using the O$_3$ cross section[19] $\sigma = 1.15 \times 10^{-17}$ cm^2. This concentration was scaled by the appropriate ratios of pressures and flows to arrive at a concentration of O$_3$ in the flow tube of typically $(0.1-2.5) \times 10^{16}$ molecules cm^{-3}.

Two experimental approaches were employed in this work, each a separate tactic for reducing the secondary influences of HO$_2$ regeneration. In one, ^{18}O$_2$ was used in place of ^{16}O$_2$ making H^{18}O$_2$ in place of HO$_2$. ^{16}O$_2$ and ^{18}O$_2$ (Isotec/Matheson 98.8%) could be switched through a low-volume solenoid valve between experiments. The low volume of the valve preserved the purity of the ^{18}O$_2$ isotope and allowed the two isotopes to be regulated through the same needle valve. In the other approach, an OH scavenger, trifluorochloroethylene (CFC-1113), was added to the reaction mixture. The CFC-1113 (Matheson 99.0%) concentration was inferred by measuring each of the flow rates using calibrated mass flow meters and the total pressure in the flow tube. The CFC-1113 was mixed with the main N$_2$ flow, upstream from its introduction to the flow tube.

Tunable Diode Laser. The tunable diode laser (TDL) system coupled to an astigmatic Herriot cell used in these measurements has been described more completely elsewhere,[20,21] but some general comments on how the apparatus works are warranted. The infrared light suitable for HO$_2$ detection was generated by using a Pb-salt laser diode housed in a liquid nitrogen Dewar.

The output from the laser system was collected with a reflecting microscope objective and directed into the multipass cell. For the work presented here, the multipass cell was configured for 366 passes, which provided 201 m of total path length. The exit beam was directed to an HgCdTe photoconductive detector. The data acquisition is based on a rapid current sweep of the diode laser with synchronous detection of the transmitted radiation. For the work presented here, the 120 point spectra spanning the features of interest were acquired at a rate of 2.5 kHz. The 300 kHz analog-to-digital conversion rate is fast enough to minimize the impact of low-frequency amplitude noise.

HO$_2$ lines near 1407 cm^{-1} were used in this work with the current ramp adjusted so that the laser frequency range spanned ~0.15 cm^{-1}. This was wide enough to include four H^{16}O$_2$ lines and two H^{18}O$_2$ lines in a single laser sweep. The infrared spectroscopy of H^{16}O$_2$ has been previously investigated.[22-26] The line strengths determined by Zahniser et al.[25] and the pressure broadening coefficients determined by Nelson and Zahniser[26,27] are tabulated in the most recent HITRAN data compilation.[28]

To measure the relative line strengths and positions for H^{18}O$_2$, equal amounts of ^{18}O$_2$ and normal O$_2$ were mixed and added to trace amounts of H atoms injected into the multipass cell. The assignments of peak positions and line strengths for H^{18}O$_2$ are given in Table 1. For the pseudo-first-order kinetic measurements presented here the absolute accuracy of the line strengths is of secondary importance.

Figure 2 shows two traces of the transmitted light as a function of wavenumber: one where isotopically normal HO$_2$ is present and another for H^{18}O$_2$. The spectra shown in this figure were acquired by modulating the H atom microwave discharge source (1 s on, 1 s off) and taking the ratio of the spectra. This ratio method removes optical fringes due to scattered light in the multipass cell. The absolute H^{16}O$_2$ and

TABLE 1: Line Positions and Strengths for HO$_2$ and H^{18}O$_2$

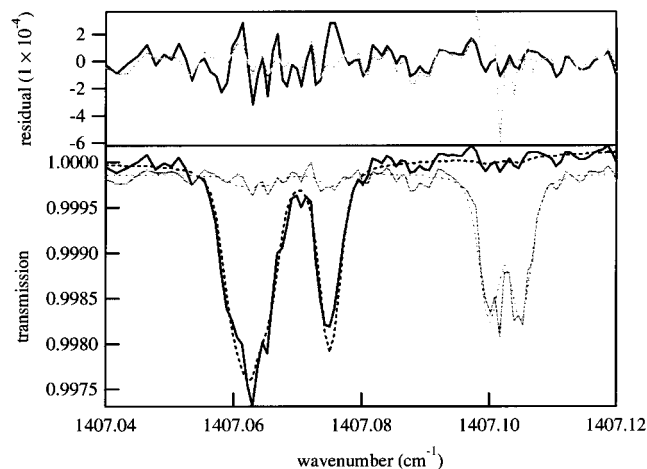| species	line wavenumber (cm^{-1})	line strength (10^{-21} cm^2 molecule^{-1} cm^{-1})	transition $N'_{K'a,K'c} \leftarrow N'_{K'a,K'c}$	references
HO$_2$	1407.063	3.4	F$_1$ [$6_{2,5} \leftarrow 5_{2,4}$]	Zahniser et al.[25]
	1407.066	4.7	F$_2$ [$7_{1,7} \leftarrow 6_{1,6}$]	and Nagai et al.[36]
	1407.069	3.4	F$_1$ [$6_{2,4} \leftarrow 5_{2,3}$]	are tabulated in the
	1407.078	5.5	F$_1$ [$7_{1,7} \leftarrow 6_{1,6}$]	HITRAN[28] database
H^{18}O$_2$	1407.103	5.0		this work
	1407.108	5.0		
	1410.968	5.6		
	1410.983	5.0		
	1411.031	5.3		
	1411.043	5.1		
	1411.101	2.6		
	1411.113	2.8		

Figure 2. H^{16}O$_2$ and H^{18}O$_2$ transmission spectra. The solid lines are the data while the dashed lines are the least-squares fits. The black data are H^{16}O$_2$ and the gray data are H^{18}O$_2$. The concentration of each species is ∼5 × 10^{10} molecules cm^{-3} in the multipass cell. The residuals of the fit have an rms absorbance of 1 × 10^{-4}.

Figure 3. Velocity profile measurements. Results of the Pitot tube measurements of the flow velocity as a function of radial distance from the center of the flow tube at three injector positions are displayed. The average flow velocity is displayed as a dashed line. The solid line represents an area-weighted average of the measured velocity profile of the turbulent core. The gray parabolic profile corresponds to a fully developed laminar flow and is included for comparison.

H^{18}O$_2$ concentrations were calculated by fitting the absorption feature to a Voigt line shape using the line parameters given in Table 1 and the broadening coefficients determined in earlier work.[27] The detection sensitivity with signal-to-noise ratio = 2 was 20 ppb, which corresponded to an absorbtivity of 2 × 10^{-4}, at 10 Torr in the multipass cell. At each injector position, data was collected for 20 s, which increased the detection sensitivity by a factor of 10$^{1/2}$ to a mixing ratio of 7 ppb. This corresponds to a number density of 2 × 10^{10} molecules cm^3 in the flow tube (100 Torr, 298 K).

Results and Discussion

When employing the turbulent flow reactor technique, two important considerations are assessing the magnitude of the effective dispersion coefficient, D_{eff}, and measuring the effective velocity of the turbulent core. The experiments conducted by Seeley et al.[9] have shown that D_{eff} under turbulent flow conditions becomes dominated by the small-scale turbulent mixing, and is between 50 and 500 cm^2 s^{-1} with no dependence on Reynolds number, when the flow is fully turbulent. The velocity fluctuations in the axial and radial directions are larger in fully developed turbulent flow than in laminar flow; however, they are sufficiently small compared to the average velocity so that, in the turbulent core, plug flow is nearly achieved. Also, the radial velocity fluctuations cause eddies whose sizes relative to the tube diameter are appreciable and allow for rapid radial mixing. As a result, whatever wall effects are occurring through the turbulent b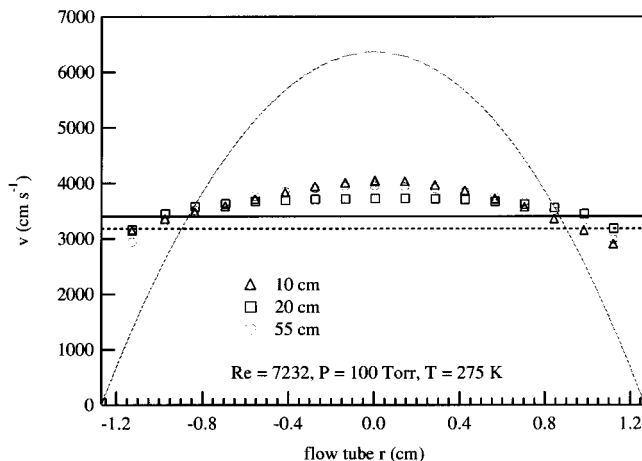oundary layer do not manifest themselves as a persistent concentration gradient across the turbulent core. Under experimental conditions typical of this work, the correction to k' due to axial diffusion, using $D_{eff} = 250$ cm^2 s^{-1}, is less than 1% and was not applied to these measurements. The magnitude of this correction is less than the uncertainty in k' that results from the uncertainty in the effective velocity determination (5%).

The second consideration when using the turbulent flow reactor lies in measuring the effective velocity of the turbulent core. An empirical relationship was developed relating the *Re* and average flow velocity to the appropriate effective velocity. This allows the effective velocity (to be used in eq 2, above) to be determined for a given average flow velocity. Some typical results of the velocity profile measurements are shown in Figure 3. Two Teflon "turbulizers" shortened the distance for turbulent flow development to less than 10 cm. The distance between the turbulizers was greater than the tooth-gap size of the turbulizers by a factor of 30 to prevent the second turbulizer from sampling a persistent stream or jet caused by the first. The initial large-scale turbulent motions caused by the second turbulizer cause vortices in the downstream flow which are on the order of the radius of the tube. The large-scale turbulence is dampened to "fully developed" turbulent flow within 10 cm, and the associated vortices are much smaller.[29] Though there are some small differences between these velocity profiles at different injector positions, no overall trend with injector position was observed. The flow velocity measurements at each measured radial position for a given flow profile were averaged with area
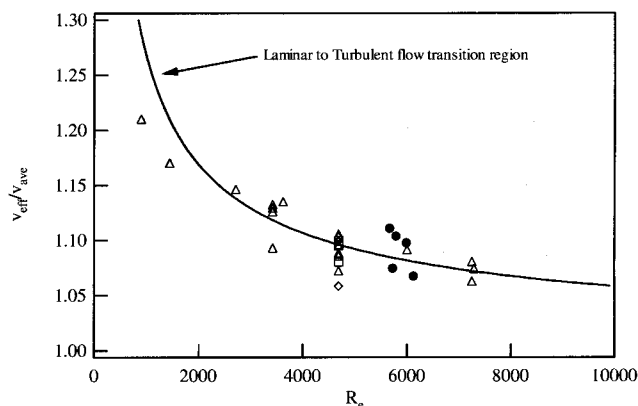
Reaction of HO$_2$ with O$_3$ from 200 to 300 K

J. Phys. Chem. A, Vol. 105, No. 9, 2001 **1587**

Figure 4. Velocity of turbulent core as a function of Reynolds number. Results of the Pitot tube velocity profile measurements are displayed. The ratio of the area weighted effective velocity to the average velocity is plotted as a function of *Re*. Data are shown for the following conditions: open triangles, 100 Torr; open circles, 50 Torr; open squares, 200 Torr. The solid circles were taken at the same injector position, but the temperature was varied, from 220 to 275 K. The spread of the data about the empirical fit line is ~5% and represents a source of systematic uncertainty in the measured value of k_1.

weighting to determine the effective flow velocity (v_{eff}). The ratio of v_{eff} to the average flow velocity v_{ave} is shown in Figure 4. In some of the measurements the temperature of the gas was varied, but no trend in effective velocity with temperature was observed. The relationship between the quantity v_{eff}/v_{ave} to *Re* was found to be $1 + 25.7/Re^{0.661}$ and is depicted by the solid line. These data show a slightly different power dependence for the Reynolds number than that predicted by theory.[30] The empirical function is used to estimate the effective core velocity used in eq 2. Note that for *Re* > 2200 (the lowest used in this work), the difference between the average velocity and that of the turbulent core is approximately 15%.

Kinetics Measurements H$_{18}$O$_2$ Isotope Measurements. The first approach adopted in this work for measuring k_1 without interference from HO$_2$ regeneration was to use isotopically labeled HO$_2$. The inner injector delivered H atoms to the outer injector (see Figure 1), where either O$_2$ or ^{18}O$_2$ was present, generating HO$_2$ or H^{18}O$_2$ via the following two reactions.

$$H + O_2 \xrightarrow{M} HO_2 \tag{R3a}$$

$$H + {}^{18}O_2 \xrightarrow{M} H^{18}O_2 \tag{R3b}$$
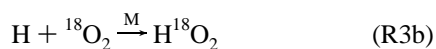
H^{18}O$_2$ is not regenerated by reaction R2 due to the very low abundance of ^{18}O in normal O$_3$. Figure 5 depicts the observed H^{16}O$_2$ and H^{18}O$_2$ concentrations for the two sources in the presence of 1.2 × 10^{16} molecules cm^{-3} O$_3$, as a function of injector distance. When the source of HO$_2$ is (R3a), the concentration of H^{18}O$_2$ is zero (lower trace). H^{16}O$_2$ exhibits a slow (10 s^{-1}) decay (top trace) due to the cycling between HO$_2$ and OH while being lost to other processes (walls). This decay rate constant is independent of the amount of O$_3$ added. When the source of radicals is (R3b), the H^{18}O$_2$ signal decays while the H^{16}O$_2$ signal grows in time. In this instance, H^{18}O$_2$ is not being regenerated and its loss is due to the sum of reaction with O$_3$ and loss on the walls. When the source of radicals is (R3a), the apparent decay of H^{16}O$_2$ is due to loss of radical to the walls. The ratio of H^{18}O$_2$ to H^{16}O$_2$, when using sources (R3b) and (R3a), respectively, gives a temporal decay due exclusively to k_1[O$_3$].

The reactions given below show some of the relevant processes to consider when measuring k_1 using isotopically substituted HO$_2$.
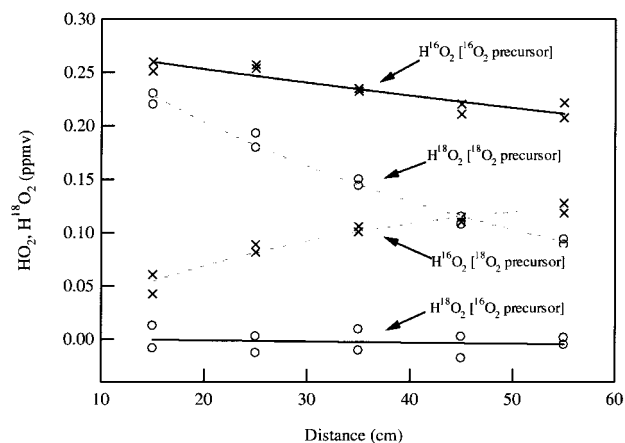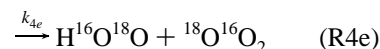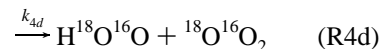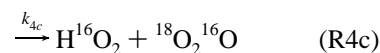

Figure 5. Temporal profiles of H^{16}O$_2$ and H^{18}O$_2$ in the presence of O$_3$. HO$_2$ mixing ratios are shown as a function of injector distance for the case where the source is H + ^{16}O$_2$ (depicted by the solid fit lines) and H + ^{18}O$_2$ (shown by the dashed lines). The × symbols are the H^{16}O$_2$ concentrations while the open circles are those of H^{18}O$_2$. These experiments were conducted at 160 Torr, 295 K, and with [O$_3$] = 1.2 × 10^{16} molecules cm^3.

$$HO_2 + O_3 \xrightarrow{k_1} OH + 2O_2 \tag{R1}$$

$$OH + O_3 \xrightarrow{k_2} HO_2 + O_2 \tag{R2}$$

$$H^{18}O_2 + O_3 \xrightarrow{k_{4a}} OH + {}^{18}O_2 + O_2 \tag{R4a}$$

$$\xrightarrow{k_{4b}} {}^{18}OH + {}^{18}O^{16}O + O_2 \tag{R4b}$$

$$\xrightarrow{k_{4c}} H^{16}O_2 + {}^{18}O_2{}^{16}O \tag{R4c}$$

$$\xrightarrow{k_{4d}} H^{18}O^{16}O + {}^{18}O^{16}O_2 \tag{R4d}$$

$$\xrightarrow{k_{4e}} H^{16}O^{18}O + {}^{18}O^{16}O_2 \tag{R4e}$$
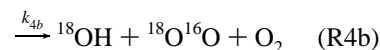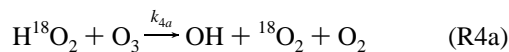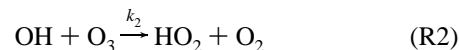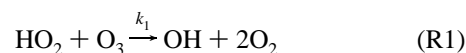
None of the listed product channels for reaction R4 has a plausible chance of regenerating H^{18}O$_2$ through an elementary reaction with normal O$_3$. The isotopic scrambling reactions (R4c−R4e) have also been shown to be small[7] and contribute <2% to the total, k_4. Isotopic exchange between the O$_3$ and ^{18}O$_2$ in the flow reactor would complicate this measurement, by opening a possible regeneration of H^{18}O$_2$ via reaction of ^{18}OH with ^{18}O$-^{16}$O$_2$ present in the reactor. The exchange between molecular oxygen and ozone has been shown to be very slow.[31,32] Assuming the most favorable conditions for this source of H^{18}O$_2$ regeneration, the amount of ^{18}O^{16}O$_2$ would be 0.01% of the total O$_3$. The natural abundance of the ^{18}O isotope (0.2%) is much greater than the amount formed by scrambling between ^{18}O$_2$ and O$_3$ in the flow tube. This source of regeneration could make the apparent k_1 less than the true k_1 by less than 0.02% due to the fact that, at room temperature,[8] the ratio of k_{4b} to k_4 is <12%.

The manner of data collection while using the isotope allows for a convenient measurement of the wall loss at each O$_3$ concentration. The ratio of H^{18}O$_2$ (when (R3b) is employed) to HO$_2$ (when (R3a) is used) yields temporal decays, due exclusively to k_1[O$_3$]. The ratio of H^{18}O$_2$ to H^{16}O$_2$ taken under the circumstances described is depicted in Figure 6 vs injector distance. The figure legend gives the specific number densities of O$_3$. A coarse guide to the ozone concentration is given by the shading of the points where the darker points indicate greater O$_3$ than the lighter points. This shows temporal decays of H^{18}O$_2$
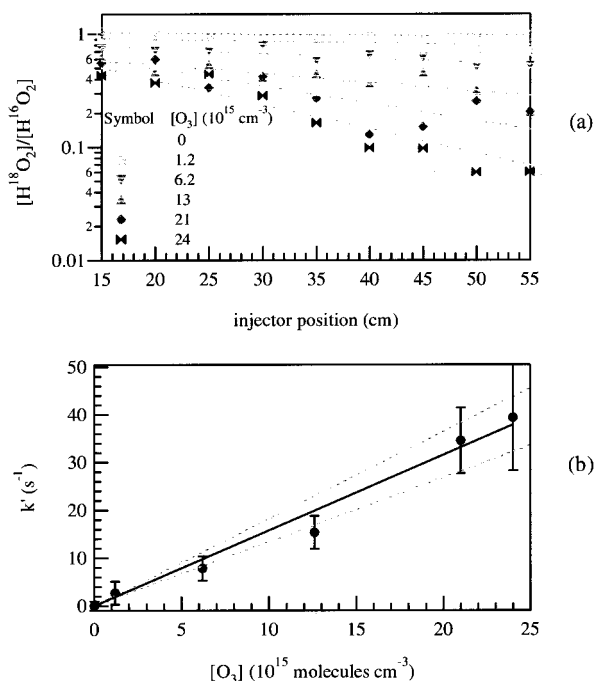
Figure 6. Temporal profiles of the ratio of $H^{18}O_2$ (R3b source) to $H^{16}O_2$ (R3a source). In the upper panel marked (a), the ratio of $H^{18}O_2$ when $^{18}O_2$ is present in the source to $H^{16}O_2$ when $^{16}O_2$ is present in the source is plotted vs injector distance. The total pressure in the reactor was 130 Torr, and the temperature was 273 K. The darker data points are indicative of greater $[O_3]$ relative to the lighter data points. The increase in the pseudo-first-order decay constant with increasing O_3 can be seen. The initial concentration of $H^{18}O_2$ and $H^{16}O_2$ was 53 ± 4 ppb for each of the decays shown in the figure. In the lower panel marked (b), the corresponding k' vs $[O_3]$ plot is shown.
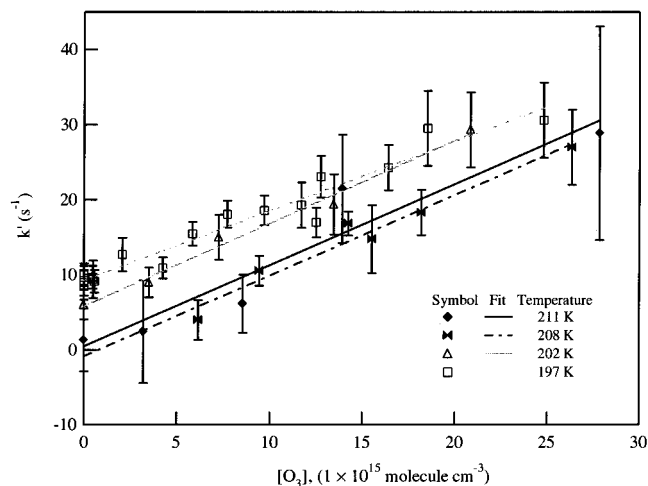

Figure 7. k' vs $[O_3]$. Measured pseudo-first-order decay coefficients vs ozone concentration are plotted for the experiments conducted between 197 and 211 K. The solid points were measured using the isotope technique, where the decay is determined from $H^{18}O_2/H^{16}O_2$, and as a result these decays have a zero intercept. The open data points are the total decays measured using the OH scavenger where the wall loss of HO_2 shows as the positive intercept ($6-12$ s^{-1}).

relative to the null or cycling $H^{16}O_2$ increase with O_3 concentration. The pseudo-first-order rate constants from the temporal profiles similar to those in Figure 6 are plotted versus $[O_3]$ to determine k_1. Such a plot is given in Figure 7, which shows results for both the isotope experiments conducted at 208 and 211 K. Figure 7 also shows the results for the OH scavenger experiments discussed below. The data on this figure represent the majority of the experiments conducted at temperatures lower

than any previously published results. One set of experiments (solid diamonds) performed at $T = 208$ K shows considerable imprecision relative to those conducted at $T = 211$ K (solid bow ties). The initial concentration of $H^{18}O_2$ in these two sets of experiments was 35 and 200 ppb, respectively. The data show that the ratio technique leads to a zero intercept as anticipated. The individual fit lines are shown in the legend for each temperature. A summary of the measurements using the $H^{18}O_2$ isotope is given in Table 2.

In the flow tube where $H^{18}O_2$ is formed (R3b), a small amount of $H_2^{18}O_2$ may be formed, which could regenerate $H^{18}O_2$ upon reaction with OH. The results of a simple numerical box model show that under the worst circumstances in the injector the $H_2^{18}O_2$ concentration delivered to the flow tube (1×10^{12} molecules cm^3) would result in an apparent rate constant which is 0.2% greater than the true value. The box model also predicts the intercept of the k' vs $[O_3]$ to be less than the measured wall loss. The observed intercepts in the plots of k' vs $[O_3]$ are consistent with the measured wall loss when the $H^{18}O_2$ decay is considered alone. The $H_2^{18}O_2 + OH$ mechanism is not a significant source of $H^{18}O_2$ regeneration.

When using the isotopically labeled HO_2 (R3b as the source), the ratio technique (following $H^{18}O_2$ decay) is the most straightforward way to analyze the isotope data. Product formation, however, can also yield information about k_1, i.e., the appearance of $H^{16}O_2$ when (R3b) is used as the radical source. The temporal behavior of $H^{16}O_2(t)$ can be solved directly from the rate laws for $H^{16}O_2$, $H^{18}O_2$, and OH radical with a few assumptions which greatly simplify the result. Assuming the wall loss rate constant for HO_2 is the same as that for OH, (R4a) is the only product channel in reaction R4, and $k_1 = k_4$, the result is given by

$$\frac{[H^{16}O_2]_t}{[H^{18}O_2]_0} =$$
$$\frac{1}{k_1 + k_2}(k_2 e^{-k_{wall}t} + k_1 e^{-\{(k_1+k_2)[O_3]+k_{wall}\}t}) - e^{-\{k_1[O_3]+k_{wall}\}t} \quad (4)$$

The use of this equation to describe the HO_2 temporal profile provides another measurement of k_1, to the extent that k_2 is known. Using this equation to fit k_1 to the $H^{16}O_2$ appearance is problematic, though because data collection was restricted to reaction times greater than ~5 ms with the geometry employed in the majority of this work. Nevertheless, when k_1 was used as a fixed parameter in (4) to see how well this expression predicts magnitude of formed $[H^{16}O_2]$, insight was gained into the $HO_2/OH/O_3$ cycling mechanism. Using the $H^{18}O_2$ decay channel to determine k_1 and k_{wall} and taking k_2 from ref 19, eq 4 overpredicts the amount of HO_2 generated at the 295 and 273 K data points by 18%. At the lower temperatures, 211 and 208 K, however, the agreement is much better 5%. More of the reaction is proceeding through the H atom abstraction (R4a) channel at lower temperatures than at room temperature. Alternatively, the improved agreement could be due to the wall loss coefficients for HO_2 and OH becoming closer in magnitude at low temperatures than at room temperature. In either case, the temporal behavior of $H^{16}O_2$ confirms the basic mechanism postulated for HO_x cycling.

Discharge Flow Laminar Conditions. Some initial work using isotopic substitution was performed on this apparatus using a traditional low-pressure laminar flow approach. In this instance, the multipass mirrors were physically mounted in the six-way cross at the end of the flow tube. The wall loss rate coefficient for $H^{18}O_2$ at lower temperatures was deemed too

Reaction of HO$_2$ with O$_3$ from 200 to 300 K

J. Phys. Chem. A, Vol. 105, No. 9, 2001 **1589**

TABLE 2: Temperature-Dependent Measurements of k_1

temperature (K)	pressure (Torr)	mass flow (slm)	flow velocity (cm s^{-1})	Reynolds number	no. of expts	rate constant (1×10^{-15} cm^3 molecule^{-1} s^{-1})	technique
297	4.8	0.6	370	40	4	2.25 ± 0.2	laminar ^{18}O$_2$
296	154	60	1042	3505	5	2.17 ± 0.2	scavenger
296	156	68	1186	3933	4	1.9 ± 0.2	^{18}O$_2$ isotope
295	80–171	44–54	657–1492	2524–3108	25	2.0 ± 0.2	scavenger
295	110	38	940	2186	5	2.1 ± 0.6	scavenger
273	130	44	837	2715	6	1.5 ± 0.2	^{18}O$_2$ isotope
238	174	54	675	3602	7	1.4 ± 0.3	scavenger
233	157	64	870	4317	7	1.17 ± 0.12	scavenger
225	5.3	1	391	70	2	1 ± 1.0	laminar ^{18}O$_2$
219	4.7	1	435	68	4	1.2 ± 0.2	laminar ^{18}O$_2$
211	112	49	842	3524	6	1.1 ± 0.2	^{18}O$_2$ isotope
208	138	57	792	4190	6	1.1 ± 0.6	^{18}O$_2$ isotope
204	4.2	0.9	430	55	4	0.9 ± 0.9	laminar ^{18}O$_2$
202	108	44	755	3284	5	1.1 ± 0.2	scavenger
197	98–141	49–59	627–902	3712–4467	15	0.92 ± 0.2	scavenger

great to measure k_1 using the laminar flow method with the desired accuracy and led to the application of the turbulent flow being sampled into the multipass cell as shown in Figure 1. The data from these measurements are designated "laminar ^{18}O$_2$" in Table 2 and are included for comparison purposes.

Kinetics Measurements: OH Scavenger. Another technique for preventing the regeneration of HO$_2$ from influencing the measured k_1 has been used in this work. In these experiments, an OH scavenger has been added to the reaction mixture.

In reaction R5, [M] refers to the number density of the bath

$$\text{OH} + \text{ClFCCF}_2 \xrightarrow{[M], k_5} \text{OH·C}_2\text{F}_3\text{Cl} \qquad \text{(R5)}$$
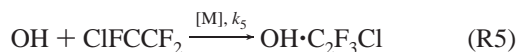
gas. The results of the measurement of k at the four lowest temperatures vs [O$_3$] are shown in Figure 7. Over the pressures and flow velocities employed at $T = 197$ K, the figure shows that k_1 is invariant. The dashed line represents the fit to all of the compiled data at 197 K. The results of this work at all temperatures are summarized in Table 2, and in the technique column, "scavenger" refers to the addition of C$_2$F$_3$Cl to the reaction mixture.
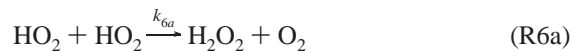
The rate constant for reaction R5 in 7 Torr of He at room temperature[33] is 6×10^{-12} cm^3 molecule^{-1} s^{-1}. The rate constant exhibits some bimolecular and termolecular character. The previously measured value is assumed to be a lower limit for k_5, as these experiments employ ~100 Torr of N$_2$ as the bath gas. In this work, experiments where the scavenger concentration was varied did not indicate any dependence of the rate coefficient measurements with the scavenger concentration >5 $\times 10^{14}$ molecules cm^3. The concentration of C$_2$F$_3$Cl was at least 3×10^{15} molecules cm^{-3} in the scavenger experiments reported here. At the highest concentrations of O$_3$ and the highest temperatures in this study, the measured rate coefficient, k, would be influenced by regeneration by at most 2%. A previously reported[4] upper limit for the reaction of HO$_2$ with C$_2$F$_3$Cl is 2×10^{-16} cm^3 molecule^{-1} s^{-1} which at the concentrations used in these experiments would represent a pseudo-first-order loss of HO$_2$ of <1 s^{-1}. This effect would not vary with O$_3$ and is not anticipated to have an effect on the measurement of k_1.

There are two possibilities for the OH·C$_2$F$_3$Cl complex. The first possibility is the ejection of a Cl atom.[33] Were this to occur, the Cl atom would react with O$_3$, forming ClO. The rate constant for the reaction of ClO with HO$_2$ is great enough to be of concern despite the low concentration of ClO. The second possibility for the excited adduct is the stabilization of the

complex and subsequent reaction with O$_2$ to form a halogenated peroxy radical.[33] At the pressure and number density of O$_2$ employed in this work, this is expected to be the dominant channel and ejection of a Cl atom is unlikely.

The measured value of k_1, using the isotope and scavenger techniques, agrees at both room temperature and low temperatures (197–211 K). This suggests that the secondary chemistry sources unique to each technique are negligible contributors to the measured values of k_1.

Self-Reaction. At the number densities of HO$_2$ employed in the flow tube, typically less than 4×10^{11} molecules cm^{-3}, the self-reaction could be significant. The total rate constant for the HO$_2$ self-reaction consists of bimolecular and termolecular components, shown below.

$$\text{HO}_2 + \text{HO}_2 \xrightarrow{k_{6a}} \text{H}_2\text{O}_2 + \text{O}_2 \qquad \text{(R6a)}$$

$$\xrightarrow{[M], k_{6b}} \text{H}_2\text{O}_2 + \text{O}_2 \qquad \text{(R6b)}$$

The rate constant for the self-reaction of HO$_2$, reaction R6 at 200 Torr and 298 K, is ~2×10^{-12} cm^3 molecule^{-1} s^{-1} and increases with decreasing temperature. A simple numerical box model was constructed to ascertain the effects of reaction R6 on the measurement of k_1. The model was used to construct temporal HO$_2$ data considering reactions (R1, R2, and R5), then again with (reaction R6) added to the model. These data were fit, neglecting the initial times due to the flow tube end effect (approximation time < 10 ms). The result of these model trials for the greatest amounts of initial HO$_2$ (1×10^{12} molecules cm^{-3}) was that the apparent or measured k_1 would be up to 5% lower than the true k_1 at 195 K (1% at 298 K). The model also predicts that in zero O$_3$, the apparent first-order decay rate constant would be greater than that chosen for the wall. The results from the isotope experiments give an effective k_{wall} which does not change with [O$_3$]. As a result, reaction R6 does not have a significant impact on the results within the precision of these measurements. The measured values of the rate constant have not been corrected by the small percentage predicted by the model.

Several variations in pressure and flow velocity were performed at room temperature using the scavenger technique. The measured rate constant showed no systematic trend with these variations. This lends additional confidence that the turbulent core velocity correction function (see Figure 4) is not introducing a systematic bias that is greater than the precision of the apparatus.

TABLE 3: Rate Constant Parameters for This and Previous Work (measurements of k_1)

temperature range (K)	pressure (Torr)	A (1×10^{-15} cm^3 molecule^{-1} s^{-1})	E_a/R (K^{-1})	C (1×10^{-15} cm^3 molecule^{-1} s^{-1})	technique	reference
245−365		14 ± 4	580 ± 100		DF-LMR	Zahniser et al.[4]
243−413	2.0−3.2	38 ± 24	820 ± 190		DF-LMR	Sinha et al.[7]
		320 ± 580	1730 ± 740	1.2 ± 0.5		
298	1.6−2.0	1.9 ± 0.3			DF-photofragment	Manzanares et al.[5]
253−400	0.5−3.0	18 ± 6	680 ± 148		DF-photofragment	Wang et al.[6]
197−300	50−230	103 ± 57	1323 ± 160	0.88 ± 0.1	TFR-TDL	this work
197−300		88 ± 35	1303 ± 116	0.9 ± 0.1		all data, $T < 300$ K

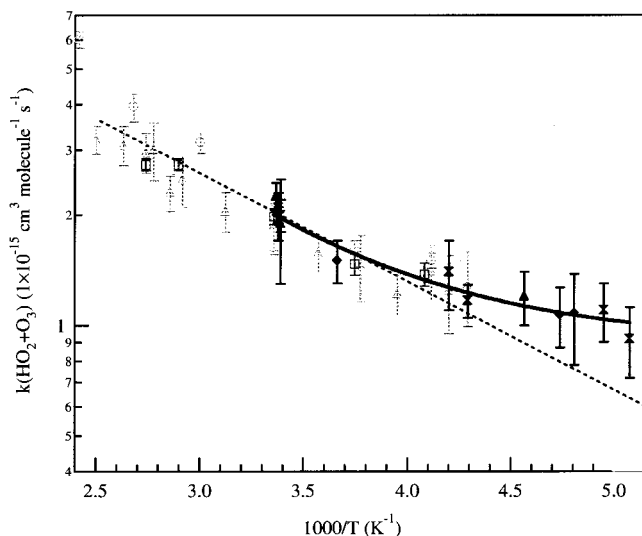**Figure 8.** Arrhenius plot for $k(HO_2+O_3)$. The measured rate constants are displayed as a function of inverse temperature. The open triangles are the data of Wang et al., the open circles are the data of Sinha et al., the open squares are the data of Zahniser and Howard, and the room-temperature measurement of Manzanares et al. is depicted as a solid square. The solid symbols represent this work. The triangles are the laminar flow measurements, the squares are the scavenger measurements, and the bow ties are the isotope measurements. The solid line represents the best fit to all the data below 300 K, using the form described in the text. The dashed line is the recommended rate constant and the shaded region represents the uncertainty in the rate constant taken from Sander et al.[35]

Comparison to Previous Measurements. The previous measurements of k_1 along with the rate constants determined in this work are shown in Figure 8 and summarized in Table 3. In Figure 8, the straight dashed line represents the current recommended rate constant for use in stratospheric modeling and the shaded area is the uncertainty in this rate constant.[35] The solid black line represents a simple fit of the combined data, $T < 300$ K, to an empirical form which is the traditional Arrhenius form, plus a constant. A fit of the data in the present work yields the expression $k_1(T) = \{(103 \pm 57) \exp[-(1323 \pm 160)/T] + 0.88\} \times 10^{-15}$ cm^3 molecule^{-1} s^{-1}, which adequately describes the curvature in the Arrhenius expression over the limited temperature range of this study.

The first observation that may be drawn from looking at Figure 8 and Table 3 is that the absolute agreement between this work and each of the previous studies is very good, within 10%. The second and most important is that k_1 exhibits non-Arrhenius behavior. At 200 K, the rate constant is 40% greater than that predicted by an Arrhenius extrapolation of the higher temperature measurements.

These results are also consistent with recently reported[34] low-temperature results for the sum of $k_1 + k_2$. This apparent agreement is not a strong confirmation of the low-temperature results, because the sum is dominated by the reaction of OH with O$_3$ (k_2).

Conclusions

This work extends the low-temperature measurements of k_1 considerably, down to 197 K. This work has used two methods, isotopic labeling and OH scavenging, for measuring k_1 directly, without appreciable influence from the regeneration of HO$_2$. Within the precision of these measurements, these two schemes agree. In the temperature range where previous measurements were available, 233−400 K, the determination of k_1 presented in this work agrees within ∼10%.

The use of the turbulent flow reactor has allowed a direct examination of k_1 at lower temperatures and higher pressures than traditional flow tube methods. Secondary chemistry in the flow tube with respect to the regeneration of H^{16}O$_2$ and/or or H^{18}O$_2$ via reaction R2 and other possibilities has been shown to be well understood and not a significant source of error. The turbulent flow reactor technique has been shown to be capable of measuring rate constants for other systems.[11,12] The agreement of this work with other measurements of k_1 gives further confidence that the turbulent flow reactor technique can be employed to measure gas-phase rate constants.

To determine an expression for use in stratospheric modeling, a simple fit of all data was done (this work and the previous direct measurements of k_1 for $T < 300$ K). The empirical form of the expression chosen is the Arrhenius expression plus a constant and results in $k_1(T) = \{(88 \pm 35) \exp[-(1303 \pm 116)/T] + 0.9\} \times 10^{-15}$ cm^3 molecule^{-1} s^{-1}.

These measurements show that k_1 exhibits non-Arrhenius behavior. The rate constant for the O atom transfer (terminal O on HO$_2$) channel has been previously shown[8] to be a small fraction of the total rate constant at low temperatures and is not responsible for the observed curvature. It remains possible that at low temperatures new uninvestigated channels open up or that H atom tunneling becomes significant.

References and Notes

(1) Wennberg, P. O. *Science* **1994**, *266*, 398.
(2) Cohen, R. C.; Wennberg, P. O.; Stimpfle, R. M.; Koplow, J.; Anderson, J. G.; Fahey, D. W.; Woodbridge, E. L.; Keim, E. R.; Gao, R. S.; Proffitt, M. H.; Loewenstein, M.; Chan, K. R. *Geophys. Res. Lett.* **1994**, *21*, 2539−2542.
(3) Lanzendorf, E. J.; Hanisco, T. F.; Stimpfle, R. M.; Anderson, J. G.; Wennberg, P. O.; Cohen, R. C.; Gao, R. S.; Margitan, J. J.; Bui, T. P. *J. Phys. Chem. A*, this issue.
(4) Zahniser, M. S.; Howard, C. J. *J. Chem. Phys.* **1980**, *73*, 1620.
(5) Manzanares, E. R.; Suto, M.; Lee, L. C. *J. Chem. Phys.* **1986**, *85*, 5027−5034.
(6) Wang, X.; Suto, M.; Lee, L. C. *J. Chem. Phys.* **1988**, *88*, 896−899.
(7) Sinha, A.; Lovejoy, E. R.; Howard, C. J. *J. Chem. Phys.* **1987**, *87*, 2122−2128.
(8) Nelson, D. D.; Zahniser, M. S. *J. Phys. Chem.* **1994**, *98*, 2101−2104.

Reaction of HO$_2$ with O$_3$ from 200 to 300 K

J. Phys. Chem. A, Vol. 105, No. 9, 2001 **1591**

(9) Seeley, J. V. Experimental Studies of Gas-Phase Radical Reactions Using the Turbulent Flow Tube Technique, Ph.D. Thesis, MIT, 1994.

(10) Seeley, J. V.; Jayne, J. T.; Molina, M. J. *Int. J. Chem. Kinet.* **1993**, *25*, 571−594.

(11) Seeley, J. V.; Jayne, J. T.; Molina, M. J. *J. Phys. Chem.* **1996**, *100*, 4019−4025.

(12) Seeley, J. V.; Meads, R. F.; Elrod, M. J.; Molina, M. J. *J. Phys. Chem.* **1996**, *100*, 4026−4031.

(13) Brenner, H. *Langmuir* **1990**, *6*, 1715−1724.

(14) Poirier, R. V.; Carr, R. W. J. *J. Phys. Chem.* **1971**, *75*, 1593−1601.

(15) Abbatt, J. P. D.; Demerjian, K. L.; Anderson, J. G. *J. Phys. Chem.* **1990**, *94*, 4566.

(16) Keyser, L. F. *J. Phys. Chem.* **1984**, *88*, 4750−4758.

(17) Beenakker, C. I. M. *Spectrochim. Acta* **1976**, *31B*, 483−486.

(18) Emrich, R. D. *Methods of Experimental Physics*; Academic Press: New York, 1981; Vol. 18A.

(19) DeMore, W. B.; Sander, S. P.; Golden, D. M.; Hampson, R. F.; Kurylo, M. J.; Howard, C. J.; Ravishankara, A. R.; Kolb, C. E.; Molina, M. J. "Chemical Kinetics and Photochemistry Data for Use in Stratospheric Modeling;" Jet Propulsion Laboratory, 1997.

(20) McManus, J. B.; Kebabian, P. L.; Zahniser, M. S. *Appl. Opt.* **1995**, *34*, 3336−3348.

(21) Zahniser, M. S.; Nelson, D. D.; McManus, J. B.; Kebabian, P. L. *Philos. Trans. R. Soc. London A* **1995**, *351*, 371−382.

(22) Saito, S.; Matsumura, C. *J. Mol. Spectrosc.* **1980**, *80*, 34−40.

(23) Paukert, T. T.; Johnson, H. S. *J. Chem. Phys.* **1972**, *56*, 2824−2838.

(24) Buchanan, J. W.; Thrush, B. A.; Tyndall, G. S. *Chem. Phys. Lett.* **1983**, *103*, 167−168.

(25) Zahniser, M. S.; McCurdy, K. E.; Stanton, A. C. *J. Phys. Chem.* **1989**, *93*, 1065−1070.

(26) Nelson, D. D.; Zahniser, M. S. *J. Mol. Spectrosc.* **1991**, *150*, 527−534.

(27) Nelson, D. D.; Zahniser, M. S. *J. Mol. Spectrosc.* **1994**, *166*, 273−279.

(28) Rothman, L. S.; Rinsland, C. P.; Goldman, A.; Massie, S. T.; Edwards, D. P.; Flaud, J.-M.; Perrin, A.; Camy-Peyret, C.; Dana, V.; Mandin, J.-Y.; Schroeder, J.; McCann, A.; Gamache, R. R.; Wattson, R. B.; Yoshino, K.; Chance, K. V.; Jucks, K. W.; Brown, L. R.; Nemtchinov, V.; Varanasi, P. J. *Quant. Spectrosc. Radiat. Transfer* **1998**, *60*, 665−710.

(29) Sullivan, P. J. *J. Fluid Mech.* **1971**, *49*, 551−576.

(30) White, F. M. *Fluid Mechanics*; McGraw-Hill: New York, 1979.

(31) Anderson, S. M.; Morton, K.; Mauersberger, K.; Yung, Y. L.; DeMore, W. B. *Chem. Phys. Lett.* **1992**, *189*, 581.

(32) Anderson, S. M.; Morton, J.; Mauersberger, K. *Geophys. Res. Lett.* **1987**, *14*, 1285.

(33) Howard, C. J. *J. Chem. Phys.* **1976**, *65*, 4771.

(34) Nizkorodov, S. A.; Harper, W. W.; Blackmon, B. W.; Nesbitt, D. J. *J. Phys. Chem.* **2000**, *104*, 3964−3973.

(35) Sander, S. P.; Friedl, R. R.; DeMore, W. B.; Golden, D. M.; Kurylo, M. J.; Hampson, R. F.; Huie, R. E.; Moortgat, G. K.; Ravishankara, A. R.; Kolb, C. E.; Molina, M. J. "Chemical Kinetics and Photochemistry Data for Use in Stratospheric Modeling, Supplement to Evaluation 12: Update of Key Reactions," Jet Propulsion Laboratory, 2000.

(36) Nagai, K.; Y., E.; Hirota, E. *J. Mol. Spectrosc.* **1981**, *89*, 520.